Substrate temperature and strain during sputter deposition of aluminum on cast borosilicate glass in a Gemini Observatory coating chamber

Jacques Sebag,[1,*] John Andrew,[1] Douglas Neill,[1] and Michael Warner[2]

[1]National Optical Astronomy Observatory, 950 North Cherry Avenue, Tucson, Arizona 85719, USA

[2]Cerro Tololo Inter-American Observatory, Casilla 603, La Serena, Chile

*Corresponding author: jsebag@noao.edu

Received 15 March 2010; revised 15 July 2010; accepted 22 July 2010;
posted 22 July 2010 (Doc. ID 125493); published 18 August 2010

Temperature and strain measurements obtained during coating of spin-cast borosilicate samples are presented here with an analysis of these results. These tests were performed for the Large Synoptic Survey Telescope (LSST) project to verify the possible use of sputtering deposition of optical coating on its large 8.4 m diameter primary–tertiary mirror. Made of spin-cast borosilicate glass, the working stress of the mirror's nonpolished surfaces is 100 psi (0.69 MPa), resulting in a local temperature difference limit of 5 °C. To ensure representative environmental conditions, the tests were performed in the Gemini Observatory coating chamber located in Hawaii, whose design was utilized to develop the LSST coating chamber design. In particular, this coating chamber is equipped with linear magnetrons built with cooled heat shields directly facing the mirror surface. These measurements have demonstrated that it will be safe for the LSST to use a magnetron sputtering process for coating its borosilicate primary–tertiary mirror.

OCIS codes: 310.0310, 310.1860, 310.3840, 310.4925.

1. Introduction

The Large Synoptic Survey Telescope (LSST) optical design is based on a three-large-mirror system to meet the aperture and field-of-view requirements of the scientific survey [1]. It is composed of an 8.4 m diameter borosilicate monolithic primary–tertiary mirror fabricated at the Steward Observatory Mirror Laboratory using their spin-cast process [2]. The characteristics of borosilicate glass are provided in Table 1.

The use of mirror coatings with higher reflectivity and durability than bare aluminum would significantly benefit the LSST science by increasing its overall throughput and improving its operational efficiency [3]. Because these advanced coatings require materials that do not evaporate easily and greater layer thickness and uniformity control than can be applied by conventional evaporative techniques, sputter coating must be utilized.

Sputter coating the 8.4 m diameter primary–tertiary mirror provides a significant challenge even though such coatings have been achieved for this size aperture. Coating chambers have been successfully implemented using the sputtering deposition method for large astronomical mirrors fabricated from Ultra-Low-Expansion (ULE) and Zerodur [4,5]. The Gemini Observatory successfully operates two large coating chambers (one in Hawaii and one in Chile) to coat its 8.1 m ULE primary mirrors with a protected-silver recipe. However, all previous large-diameter cast borosilicate mirrors have only been coated with bare aluminum in evaporative coating chambers [6].

0003-6935/10/244610-11$15.00/0

Table 1. Borosilicate Glass Characteristics

Young's Modulus E	Thermal Diffusivity	Coefficient of Thermal Expansion (CTE)	Specific Heat
8.5×10^6 lb/in.^{2}(58.6 GPa)	7.11×10^{-7} m^2/s	28×10^{-7}/K	710 J/kg C

Sputter coating differs from conventional evaporation techniques in how the coating material is vaporized. In the process of sputtering, the ejection of particles from the condensed-matter target is due to bombardment with high-energy ions. The most common method of providing ion bombardment is to backfill the coating chamber with a continuous flow of argon gas and to establish a glow discharge. The positive ions passing from the plasma volume impact the target (cathode) after being accelerated by the strong electric fields. A detailed description of the sputter deposition process is given in [7].

Most of the energy used in the sputtering system is removed in the form of heat from the target. A small percent of this energy is transferred in the form of electrons and ions to produce a substrate heat load. Because the process is conducted in a vacuum, convection is negligible, but substantial heating of the substrate is possible. Although there are several available configurations for sputtering, most sputtering for astronomical optics applications utilizes a direct-current (DC) system with direct cooling to the target. The DC system uses a single magnetron as the cathode. The configuration of a DC magnetron, combined with direct cooling, reduces the heat transfer to the substrate.

The LSST mirror is a cast borosilicate mirror with a faceplate 28 mm thick. This material has both a significantly higher coefficient of thermal expansion (CTE) and a lower strength than either Zerodur or ULE. Consequently, it is more susceptible to thermal damage. As a result of the fabrication process, the cast surfaces of the borosilicate mirror (BSC) are very irregular. This irregularity further decreases the strength of the material [8]. The typical breaking strength of polished borosilicate is approximately 2000 psi (13.8 MPa). The roughness of the interior surfaces, combined with the residual stress, reduces the working strength to 100 psi (0.69 MPa). Because of removal of surface flaws, the polished top optical surface of the cast borosilicate mirror can safely sustain larger stress (~3× the 100 psi limit). This reduced working strength, combined with the larger CTE, produces a maximum allowable temperature gradient of 5 °C across the mirror or through its thickness [9].

Coating tests were performed in the Gemini North Telescope coating chamber to demonstrate that sputter coating will be safe for large borosilicate mirrors. In this paper, we present the configuration and the results of these coating tests, including a modeling analysis for extrapolation to different configurations.

2. Coating Test Configuration

A. Gemini Coating Chamber

The tests discussed in this paper were performed in the Gemini Observatory coating chamber located in Hawaii. Of particular interest for these tests was the direct-cooling linear magnetron configuration with a cooled uniformity mask located in front of the target. This mask is used to control the layer thickness uniformity while the mirror rotates below the magnetron to compensate for the mirror's radial linear speed variation. There was also a cooled shutter between the target and the mask to control precisely the area to be coated on the mirror to obtain uniform coating thickness. Cooling was provided to these components by a 30 gal/min (0.114 m^3/min) water coolant flow at an input temperature of 9 °C. When the magnetron was not active, the coolant return temperature was 14 °C, which corresponds to a 40 kW cooling capacity relative to ambient conditions. During coating, the coolant temperature climbed to 21 °C, which represents an additional cooling load equal to 53 kW.

Both cooled shields play an important role during sputtering because they are located directly above the mirror. For these tests, the distance between the target and the sample was approximately 100 mm, and the distance between the mask and the sample was approximately 25 mm. Similar distances are expected to be utilized in the LSST coating chamber.

The Gemini chamber was built with the capability of sputter depositing aluminum, which was used on the Gemini primary mirror for their initial coatings. Three Advanced Energy 20 kW Pinnacle power supplies are available for this purpose. Aluminum was chosen for these thermal tests because it requires more power during deposition and represents a worst-case thermal scenario. Moreover, LSST may also deposit aluminum on its mirrors. Gemini has used a maximum of 40 kW power level for aluminum coatings. The original plan was to execute the thermal test at this maximum power and to deposit an aluminum layer thickness of 100 nm within one pass under the magnetron. However, arcing in the magnetron prevented us from reaching that level and, instead, power delivered to the magnetrons was limited to 10 kW during the tests. This limitation was overcome for the tests by decreasing the rotation speed of the samples to obtain the expected layer thickness. Moreover, temperature modeling, discussed later in this paper, was developed to extrapolate these tests results to higher power levels.

Table 2. Samples Properties

Thickness (mm)	Dimensions and Mass	Surface	Material	Plate (Quantity)
2	152.4 × 152.4 mm^2 112 g	Polished	Float	A(1)
12.7	50.8 × 50.8 mm^2 75 g	Polished	Pyrex	A(3), B(4), C(4)
28	165 mm radius 1.3 kg for B and 0.7 kg for C	Polished (B) and Rough (C)	BSC	B(1), C(1)

B. Sample Configuration

Three types of samples were used for these tests with different substrate sizes and thicknesses (see Table 2). The 28 mm thickness was chosen as it corresponds to the design thickness of the LSST mirror's face plate. One of these samples also had a polished front surface representative of the LSST optical surface, while the other sample had a rough front surface more representative of the irregularities of the nonpolished surfaces. The shape of the two 28 mm thick BSC samples was not identical. The sample on plate B had a uniform thickness of 28 mm, representative of the LSST face plate. The sample on plate C had a variable radial thickness decreasing from 28 mm at the edge to 8 mm at the center along a spherical shape on the back side.

The samples were distributed on three different test plates. The first test plate (identified as plate A) was composed of the 2 mm thick sample and 3 mm × 12.7 mm thick Pyrex samples. The other samples were distributed on two identical plates (identified as plates B and C) each composed of four Pyrex samples and one cast borosilicate sample (Fig. 1). Before each run, a shield plate was placed just above the samples to protect the sensor cables and to define a precise aperture above each sample. The same shield plate was used for the three coating runs, as only one plate was tested per run.

C. Sensor Configuration

Temperature and strain sensors were bonded on the samples:

– Platinum resistance temperature detector (RTD) surface mount F3102 temperature sensors from OMEGA
– Delta rosette CEA-03-250UY-350 strain gauges from VISHAY

The distribution of sensors per test plate is given in Table 3. Platinum surface RTDs were chosen for this test because they have a short response time to react to changes in surface temperature. This factor was important to ensure an accurate monitoring of the temperature change as the sample rotates below the magnetron. A three-element 120° delta rosette strain gauge was selected for the determination of the principal stresses. The temperature sensors were considered the prime sensors for this experiment and were installed on all the front and back surfaces of every sample. The strain gauges were installed solely on the large borosilicate samples and on the thin float glass sample. When both sensors were placed on the same samples, the strain gauges were located toward the center of the samples and the temperature sensors away from the strain gauges. The strain gauges are resistive elements that dissipate negligible heat (~3 mW), slightly increasing the temperature of the samples during the tests. Also, small soldering contact strips were used to avoid any effect of the sensor cables on the measurements. After applying these precautions, each sensor was tested individually and then all the contacts were covered with kapton to prevent any short circuit during the coating.

All the sensors were connected to their acquisition electronics located inside the coating chamber in a sealed enclosure. This enclosure was held at a pressure of 1 atm during the test. The electronics were designed to monitor 12 external strain gauges and 12 external RTD temperature sensors. The test results were monitored remotely via ethernet and collected at a temporal frequency of 1 Hz.

Four ADAM ethernet I/O modules were installed inside the sealed electronics enclosure. The first two I/O modules were ADAM-6015, which are able to read seven RTD temperature sensors each, and were configured to read the 12 test temperatures, plus the temperature inside the enclosure, within a range of −50 °C to +150 °C. The second two I/O modules were ADAM-6017 configured to read 12 strain gauges, a strain gauge reference voltage, and a pressure sensor (Honeywell SDX-30A2) used to monitor the pressure inside the sealed enclosure.

The strain gauges were configured in a 1/4 bridge configuration, using a set of precision resistors, and were amplified by a factor of 100, using LTC1100 high-precision instrumentation amplifiers mounted on a circuit board. This configuration yielded an

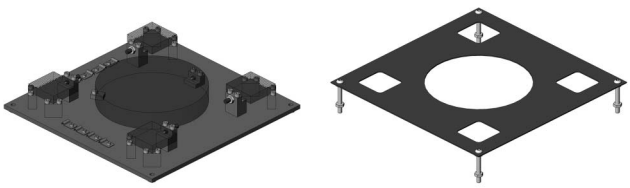

(a) (b)

Fig. 1. Test plate B with (a) samples and (b) reusable protective shield.

Table 3. Distribution of Sensors Per Test Plate

	Plate A	Plate B	Plate C
Temperature Sensors	6	12	12
Strain Gauges	2	4	4

effective scale factor of 0.5 mV/μstrain at the ADAM-6017 input or 2 μstrain/mV to transform a measured voltage into a strain value.

The other components inside the enclosure were three power supplies and a four-channel ethernet hub. Two power supplies generated +/ – 5 Vdc, which was used as the strain gauge reference voltage and to power the LTC1100 amplifiers. One +12 Vdc supply was used to power the four ADAM modules and the ethernet hub.

The enclosure external interfaces consisted of four hermetic connectors: two used to connect to the test samples sensors, one connected to +115 VAC, and the last one connected to the ethernet for remote monitoring. In addition to an electrical ground line, a copper thermal strap was also mounted on the enclosure to improve heat conduction to the coating chamber to limit the temperature rise inside the enclosure.

D. Coating Thickness

Inside the coating chamber, the Gemini Observatory mirror is normally installed on a whiffle tree that rotates the mirror under the magnetrons. For these thermal tests, the samples were placed on supports attached to that whiffle tree and located 2.6 m away from the axis of rotation. In this configuration, the positioning and alignment of the magnetron above the samples were obtained relatively rapidly, as access to the components and measurements of distances was easily done. The rotation speed was set to 0.25 rotation/h (rph) leading to a linear speed of 1.13 mm /s at a 2.6 m radius. As explained above, this choice was governed by the limitation on available power and the goal of obtaining an expected 100 nm layer thickness in one pass. The width of the mask above the sample was adjusted to 50 mm to be significantly smaller than the 165 mm diameter of the main borosilicate sample on plates B and C. This limited width enforced localized heating, which simulated the conditions of coating a large mirror and avoided edge effects. If a larger width was utilized, unrepresentative uniform heating would result, as a large area of the sample would have a uniform increase of temperature.

The Gemini chamber was equipped with quartz crystal oscillator thickness monitors attached to the whiffle tree. The thickness was measured by passing the quartz crystal sensor under the magnetron at a radius position equal to the center of the test plate radius and at the same rotation speed. Two different sensors were used for this experiment. The average thickness of 101 nm was computed from the measurements, and the deposition rate was estimated to be 2.3 nm/s.

Because of uncertainties in the transformation factor used to match the acoustic properties of the material being deposited to the acoustic properties of the quartz crystal, the thickness of some samples was remeasured after the coating tests for verification. These measurements, performed by Optical Data Associates (ODA) in Tucson, averaged to 69 nm in thickness. This value is smaller than the one estimated during the coating test, but utilizing the thinner thickness for the experiment produces the larger, worst-case temperature increase when the experimental data are extrapolated to the actual desired coating thickness.

3. Temperature Test Results and Models

The temperature measurements recorded during the three coating runs are presented here. Other than the variation in sample plate (A, B, or C), these three coating runs were identical. This section also includes a description of the models used to characterize these results. All the temperature results are summarized in Table 4.

A. Temperature Measurements

Temperature measurements and predicted results are plotted in Figs. 2–4 for each plate.

For the 2 mm thick sample [Fig. 2(a)], the temperature increased sharply, 7 °C in 80 s, to reach equilibrium. The temperature appears higher on the back surface than on the front surface due to the heat generated by the strain sensor bonded on that surface. During the passage under the magnetron, the back temperature increased 4 °C in 150 s to reach the same equilibrium temperature as the front surface.

For the 12.7 mm thick samples [Fig. 2(b)], the temperature increased 1.8 °C in 50 s on the top surface and then decreased 1 °C in 100 s to reach equilibrium. On the back surface, the temperature increased 1.2 °C in 150 s to reach the same equilibrium temperature as the front surface.

For the 28 mm thick samples [Fig. 2(c)], the measured temperature increased quickly, 2.3 °C in 50 s, on the top surface, and then decreased 1.3 °C in 250 s to reach equilibrium. On the back surface, the temperature started rising after the top surface temperature had reached its maximum and continued to increase slowly, 0.8 °C in 250 s, to reach the same temperature as the front surface.

On both large borosilicate samples, the variation of temperature was synchronized between both

Table 4. Temperature Results

	2 mm Thick	12.7 mm Thick	28 mm Thick
Measured temperature increase on top surface during coating	7 °C in 80 s	1.8 °C in 50 s	2.3 °C in 50 s
Measured temperature decrease on top surface after coating	0 °C	1 °C in 100 s	1.3 °C in 250 s
Measured temperature increase on back surface during coating	4 °C in 150 s	1.2 °C in 150 s	0.8 °C in 250 s
Predicted mean temperature increase	8.0 °C	1.4 °C	0.74 °C
Predicted front-to-back temperature difference during coating	0.58 °C	1.8 °C	2.0 °C

temperature sensors because they were located symmetrically opposite to each other on a line parallel with the linear magnetron. The results measured on the 28 mm samples show that it would be safe for the LSST mirror to be coated with aluminum by sputtering using a 10 kW power in conditions similar to the Gemini chamber.

B. Temperature Models

Thermal models were utilized to extrapolate these results to a higher power configuration or an increased layer thickness to verify that under such conditions the coating will still be safe for the LSST mirror. The variation of the mean temperature was modeled first for the different samples to compare the predicted value with the temperature difference measured between the start and the end of the coating test. This model was then extended to predict temperature variations between the front and back surfaces. Finally, the temperature decay was estimated using a conduction model since the magnetron is no longer coating the sample at this point in the process.

1. *Mean Temperature Model*

The change in mean temperature through the thickness can be predicted by an energy balance calculation [10]:

$$Q - A\sigma\varepsilon(T_1^4 - T_2^4) = mc\frac{dT}{dt}, \qquad (1)$$

where Q is the substrate heat load (W); A is the radiative area (m^2); σ is the Boltzmann constant ($W/m^2\ K^4$); ε is the emissivity (na); m is the mass (kg); c is the specific heat of the substrate (J/kg C); T is the mean temperature of the sample (K); T_1 is the temperature of the exposed surface of the sample (K); T_2 is the ambient temperature (K); t is the coating time (s).

In the energy balance, the first term Q is the energy entering the sample from the sputtering process. The second term in Eq. (1) is the energy emitted by radiation from the sample. The third term is the sample increase in thermal energy. Because the energy emitted from the sample through radiation was minimal, the front and back surface temperatures were set equal to the mean temperature to simplify the calculations. Consequently, equal energy emission was assumed for both the front and back surfaces of the sample. The values utilized for the above equation are presented in Table 5.

To determine the substrate heat load Q, an incoming substrate flux of 783 W/m^2 was first predicted using [10] and the deposition rate of 1.57 nm/s to scale their measurements. This value was then slightly reduced to 700 W/m^2 to best fit the temperature measurements.

"Ambient temperature" is used to refer to the initial temperature of the test setup before coating of the samples. The experiments were conducted on differ-

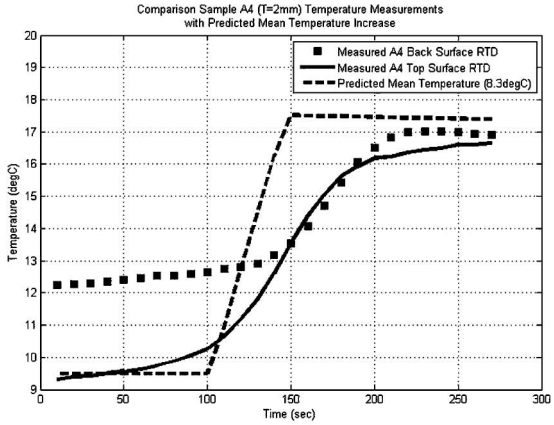

(a)

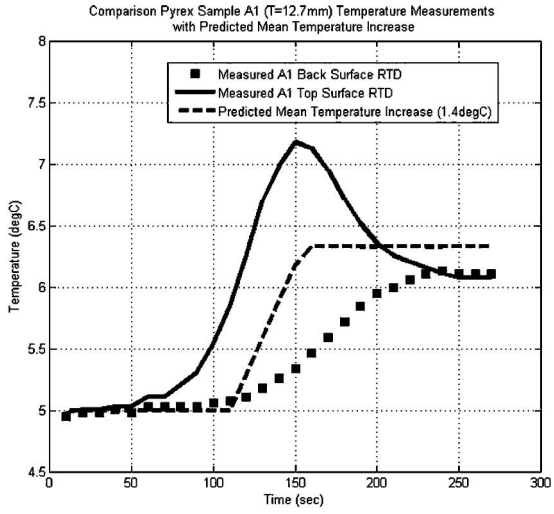

(b)

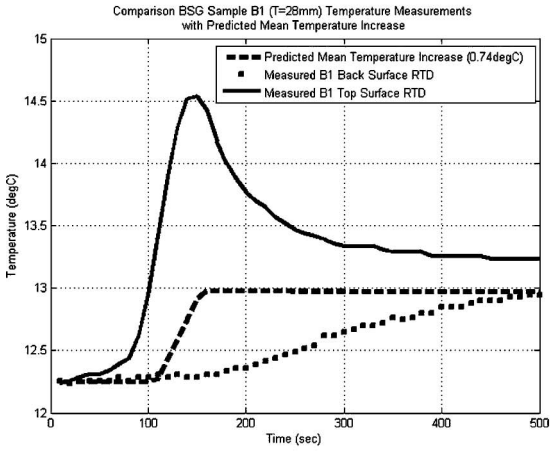

(c)

Fig. 2. Comparison of measured surface temperatures and predicted mean temperatures for samples of different thicknesses: (a) Comparison of sample A4 (thickness = 2 mm) temperature measurements with predicted mean temperature increase. (b) Comparison of Pyrex sample A1 (thickness = 12.7 mm) temperature measurements with predicted mean temperature increase. (c) Comparison of borosilicate glass sample B1 (thickness = 28 mm) temperature measurements with predicted mean temperature increase.

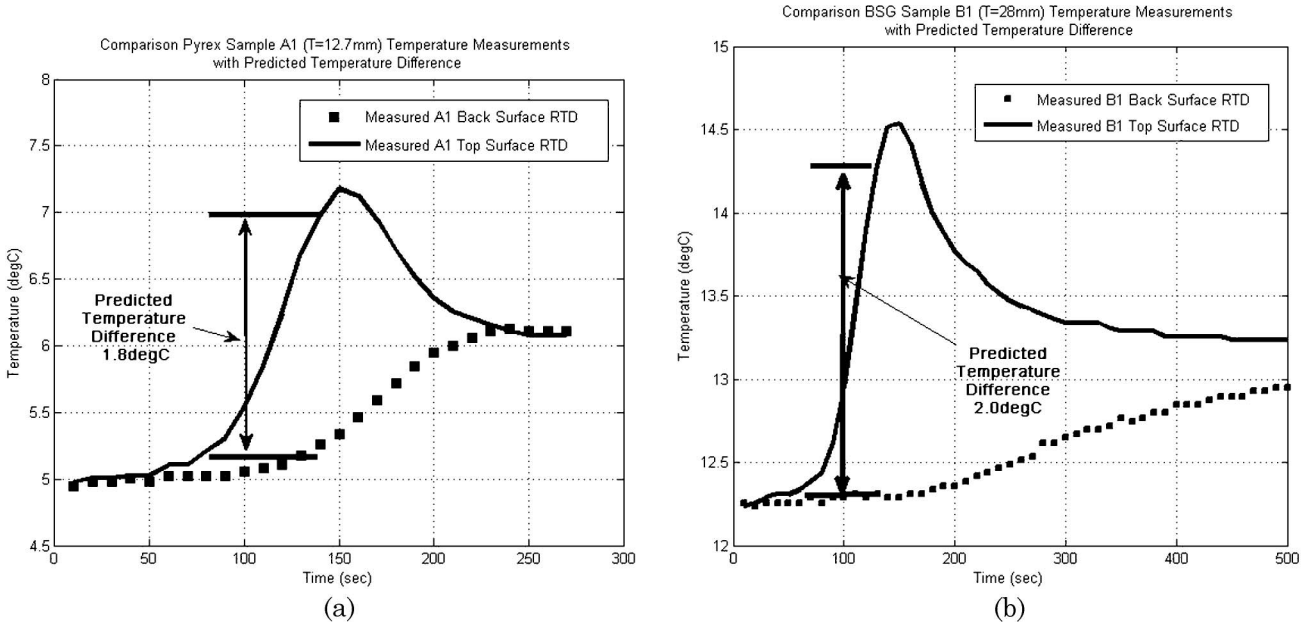

Fig. 3. Comparison of measured and predicted temperature differences: (a) Comparison of Pyrex sample A1 (thickness = 12.7 mm) measured and predicted temperature differences. (b) Comparison of borosilicate glass sample B1 (thickness = 28 mm) measured and predicted temperature differences.

ent dates and times resulting in variations in the ambient temperature. Other than the coated surface, the test setup experienced negligible ambient temperature variation during each test. For the thin sample, there is little temperature variation through the substrate thickness and the mean temperature (T) is approximately equal to the sample surface temperature (T_1). For the thicker samples, the sample surface temperature must be greater than the mean temperature as a result of a temperature gradient through the thickness. Although this gradient produces an error in the radiant transfer calculations described above, for all cases the radiative heat emitted from the sample is negligible. For example, the maximum calculated energy emitted by radiation from the 28 mm thick sample was 25 mW during the experiment, which is small in comparison with the heat load.

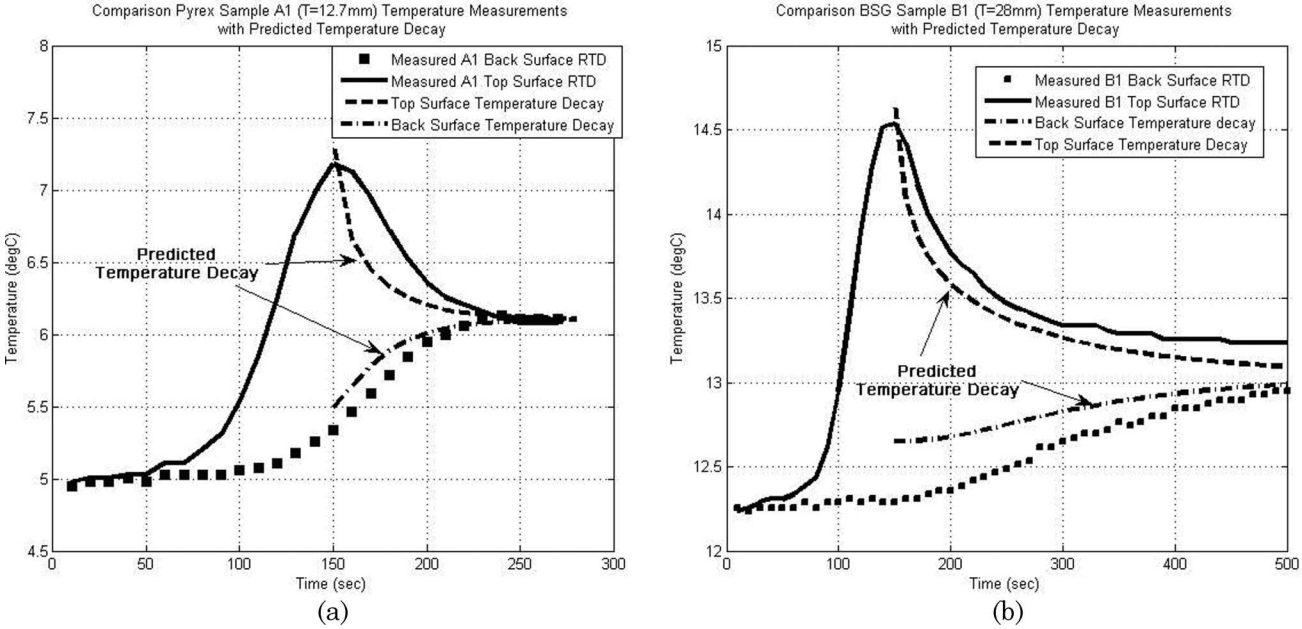

Fig. 4. Comparison of measured and predicted postcoating surface temperatures: (a) Comparison of Pyrex sample A1 (thickness = 12.7 mm) measured and predicted postcoating surface temperatures. (b) Comparison of borosilicate glass sample B1 (thickness = 28 mm) measured and predicted postcoating surface temperatures.

Table 5. Values Utilized in Calculations

Values Utilized In Calculations					
		Thickness (mm)			
Symbol	Variable	2	12.7	28	Units
Q	substrate heat load	16.26	1.81	14.97	W
A	radiative area	0.0465	0.0052	0.0428	m^2
σ	Boltzmann constant	5.67E – 08	5.67E – 08	5.67E – 08	$W/m^2\ K^4$
ε	emissivity	0.048	0.048	0.048	na
m	mass	0.112	0.075	1.30	kg
T_2	ambient temperature	282.5	278.0	285.3	K
r	density	2230	2230	2180	kg/m^3
k	thermal conductivity	1.10	1.13	1.10	W/m C
c	specific heat of substrate	830	837	710	J/kg C
α	thermal diffusivity	5.94E – 07	6.05E – 07	7.11E – 07	m^2/s
t	coating time	44	44	44	s

The predicted mean temperature increases of 1.4 °C and 0.74 °C are in general agreement with the measured temperature differences between the start and the end of the coating of 1.2 °C and 0.8 °C for the 12.7 and 28 mm thick samples, respectively [Figs. 2(b) and 2(c)]. These temperature differences are equal to the change of temperature of the sample back surfaces. For the 2 mm thick sample [Fig. 2(a)], the predicted mean temperature increase is equal to 8 °C, and the measured value is 4 °C. This difference is due to the presence of the strain gauges on the back surface of the sample. The heat generated by this resistive element increased the back temperature, making it warmer than the front surface by almost 3 °C. Without the strain gauges, the measured value would have been around 7 °C (as it is for the front surface) and in better agreement with the prediction.

2. *Gradient Temperature Model*

The previously predicted temperatures are mean values that were found in general agreement with the measured data between the start and the end of the coating. However, during the coating, a significant temperature gradient develops through the thickness for the thicker samples, and the front and back surface temperatures change at a different rate. The temperature as a function of depth "x" can be predicted by the unsteady energy balance equation:

$$Tx - T_i = 2\frac{Q}{A}\frac{\sqrt{\alpha t \pi}}{k}\exp\left(\frac{-x^2}{4\alpha t}\right) - \frac{Qx}{Ak}\left(1 - \operatorname{erf}\left(\frac{x}{2\sqrt{\alpha t}}\right)\right), \quad (2)$$

where Q is the substrate heat load (W); A is the radiative area (m^2); ρ is the density (kg/m^3); k is the thermal conductivity (W/m C); c is the specific heat of the substrate (J/kg C); α is the thermal diffusivity $\{\alpha = k/(\rho \cdot c)\}$ (m^2/s); T_x is the temperature as a function of depth (K); T_i is the initial temperature (K); t is time (s); x is the distance from the front surface (m).

The resulting temperature gradient is an exponential decay with the maximum temperature on the top surface. The mean temperature Eq. (1) provided earlier is still valid, and this mean temperature must be between the temperatures of the top and back surfaces, and closer in value to the temperature of the back surface.

Using Eq. (2), the predicted front-to-back temperature differences are found equal to 1.8 °C and 2.0 °C for the 12.7 and 28 mm thick samples, respectively. These values are in general agreement with the measured values of 2.2 °C and 2.3 °C for the 12.7 and 28 mm thick samples, respectively [Figs. 3(a) and 3(b)]. For the 2 mm thick sample, the predicted temperature difference is equal to 0.58 °C. This is not straightforwardly measurable on the data because the front and back surface temperatures changed basically simultaneously on that sample and the heat generated by the strain gauge creates a temperature difference that is much larger than 0.5 °C.

3. *Temperature Decay Model*

Both previous thermal models show a good correlation between the predicted values and the measured data from "start to end" and during the coating process. Finally, the decay of the temperature gradient was measured and modeled after the coating process was terminated to further characterize the thermal response of the samples. A significant temperature gradient exists between the front and back surfaces immediately after the coating ends. Since the samples are no longer experiencing a heat flux and radiation losses are negligible, the decay of the thermal gradient is governed entirely by conduction. This decay was modeled as a function of time of the previously determined thermal gradient by discretizing the substrate through its thickness, applying the conduction equation for each layer, and solving iteratively for each time step. For the 12.7 and 28 mm cases, the calculated time decay of the surface temperatures approximated well the measured values for both the top and back surfaces [Figs. 4(a) and 4(b)]. For the 12.7 mm thick sample, the predicted decay temperature is

equal to 1.4 °C over a 125 s time period. It is well correlated with the measured decay of 1.7 °C over a 125 s time period. For the 28 mm thick sample, the predicted decay is comparable to the measured decay as well. In this case, the predicted decay temperature is 1.8 °C over 300 s, and the measured decay temperature is 2.3 °C over the same time period. The data for the 2 mm thick sample were not used in this comparison for the reasons mentioned earlier.

4. Temperature Prediction for a 100 nm Layer Thickness

The thermal models have shown good general agreement with the measured data and they are used here to extrapolate the measured results to a set of different coating conditions. Because the actual mirror will have a face sheet 28 mm thick, only the case for a 28 mm thick sample is investigated (BSC sample on plate B). For the LSST mirror, the desired layer thickness is equal to 100 nm, obtained in one pass below the magnetrons. During the coating tests, the deposited coating thickness averaged 69 nm, which is thinner than the desired value. To increase the thickness from the measured value of 69 to 100 nm, different methods are theoretically investigated: increase the coating time by reducing the rotational speed, or increase the power to 20, 30, or 40 kW while keeping the same rotational speed.

A. Coating Time Increase

The average coating rate producing the 69 nm coating thickness was 1.47 nm/s during the tests (averaged deposition time of 47 s). Therefore, the required time to produce a 100 nm layer thickness becomes equal to 68 s with a 10 kW power level and the same test and mask configuration (deposition time increase of 21 s). Because the layer has to be deposited in one pass, the rotational speed has to be reduced to allow for a longer time transit under the magnetron. A 0.74 mm/s or 0.16 rph (one rotation in 6 h) rotational speed is required to give a 68 s transit time as long as the sample is at the same radial location. Using Eq. (2), this increase in time duration results in a 2.2 °C predicted temperature difference between the front and back surfaces. This result shows that increasing the coating time by 21 s raised the predicted temperature difference by 0.2 °C. In such conditions, it would be safe to coat the LSST mirror with this process.

B. Power Increase

Instead of increasing the time for coating the mirror (which means increasing the whole duration of the coating operation), the thicker layer can be obtained using a higher power level on the magnetron. This configuration is also interesting because higher power levels have also been shown to produce coating with better reflectance performances. In this case, the average coating rate is changed by increasing the power level, and therefore the required time to reach the 100 nm layer thickness is reduced accordingly. Table 6 summarizes the results for 20, 30, and 40 kW power level usage. For 20 kW, the coating duration equals 34 s with a rotational speed of 1 rotation per 3 h (0.32 rph). The predicted temperature difference that would result between the front and the back surface is 3.2 °C. When the power is increased to 30 kW, the average coating rate increases to 4.4 nm/s, requiring a 23 s coating duration to reach a 100 nm thickness. The rotational speed is then equal to one rotation in 2 h (0.48 rph) and the predicted temperature difference reaches 3.9 °C between the front and back surfaces of the sample. The maximum predicted temperature difference of 4.5 °C is obtained for the 40 kW power case.

Moreover, the predicted mean temperature increase of the sample is 1 °C for all three power cases because the total energy transferred is identical (as the power goes higher, the duration gets shorter). Also, the predicted decay time is comparable for all three cases (∼300 s) and the predicted temperature increase of the back surface is equal to ∼0.5 °C after the end of coating until reaching equilibrium.

All these resulting temperatures show that the range should not exceed the 5 °C safe limit even for the highest power case of 40 kW.

5. Maximum Stress Prediction from Thermal Modeling

The thermal models have shown that the predicted temperatures shall not exceed the safe temperature limit on the LSST mirror. These models allow one also to compute a predicted maximum stress due to thermal strain. The thermal strain is computed as the product of the coefficient of thermal expansion of the glass and of the local temperature change:

$$\varepsilon_{\mathrm{Th}} = \mathrm{CTE} * \Delta T, \tag{3}$$

where $\varepsilon_{\mathrm{Th}}$ is the thermal strain (μstrain); CTE is the coefficient of thermal expansion (μstrain/K); ΔT is the temperature change (K).

The stress is equal to the product of mechanical strain and the elastic modulus of the borosilicate glass:

Table 6. Predicted Impact of Power Change on Coating Process

Power (kW)	Coating Duration (s)	Rotational Speed (rph)	Predicted Front-to-Back Temperature Difference for BSC Sample (C)
10	47	0.25	2
20	34	0.32	3.2
30	23	0.48	3.9
40	17	0.64	4.5

$$S = \varepsilon_M * E, \tag{4}$$

where S is the stress (psi); ε_M is the mechanical strain (μstrain); E is Young's elasticity modulus (psi/μstrain). The maximum theoretically possible stress results when the thermal expansion is completely restrained, in which case, the thermal strain $\varepsilon_{\mathrm{Th}}$ and mechanical strain ε_M are equal in magnitude and opposite in orientation.

For these tests, the maximum theoretically possible stress occurs on the top surface and the predicted maximum theoretical stress results are plotted in Fig. 5 for the 10 and 40 kW power cases. For the 10 kW case, the predicted maximum theoretical stress reaches 45 psi (0.31 MPa) after 50 s. It is greatest for the 40 kW prediction case and it reaches a peak value just above 100 psi (0.69 MPa) for a short period of time equal to ~2 s.

In reality, all the thermal strain is not overcome by mechanical strain, so the actual stress should be below the theoretical maximum value. A typical value of 50% of the total thermal strain results in mechanical strain; hence, our model predicts that the maximum actual stress on the top surface should reach a value around 23 psi (0.16 MPa) for the 10 kW case and 50 psi (0.34 MPa) for the 40 kW case—well below the 300 psi (2.1 MPa) limit set for the polished surfaces of the large borosilicate mirror.

6. Strain Measurements During Coating Tests

Some of the samples on the different test plates were instrumented with strain gauges on both front and back surfaces to measure mechanical strain directly. Here, these measurements are compared to the stress prediction detailed above.

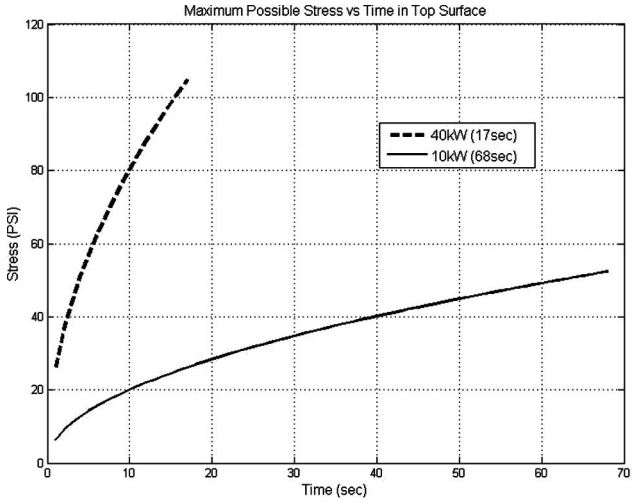

Fig. 5. Maximum possible stress versus time for 10 and 40 kW power cases.

A. Measured Signal

During the coating process, all of the strain gauges located on the top surfaces of the samples reported erratic and impossibly high strains relative to the strain limit. We believe that this was due to interference from the magnetron.

All the other strain gauges, on the back surfaces of the samples, reported realistic values except for one strain gauge on plate A. The signal analysis for these back strain gauges is described in the following paragraphs. Examples of back-surface strain measurements for plates B and C are given in Fig. 6 for the 10 kW case. These plots show the signal variations during coating of each of the three elements of the

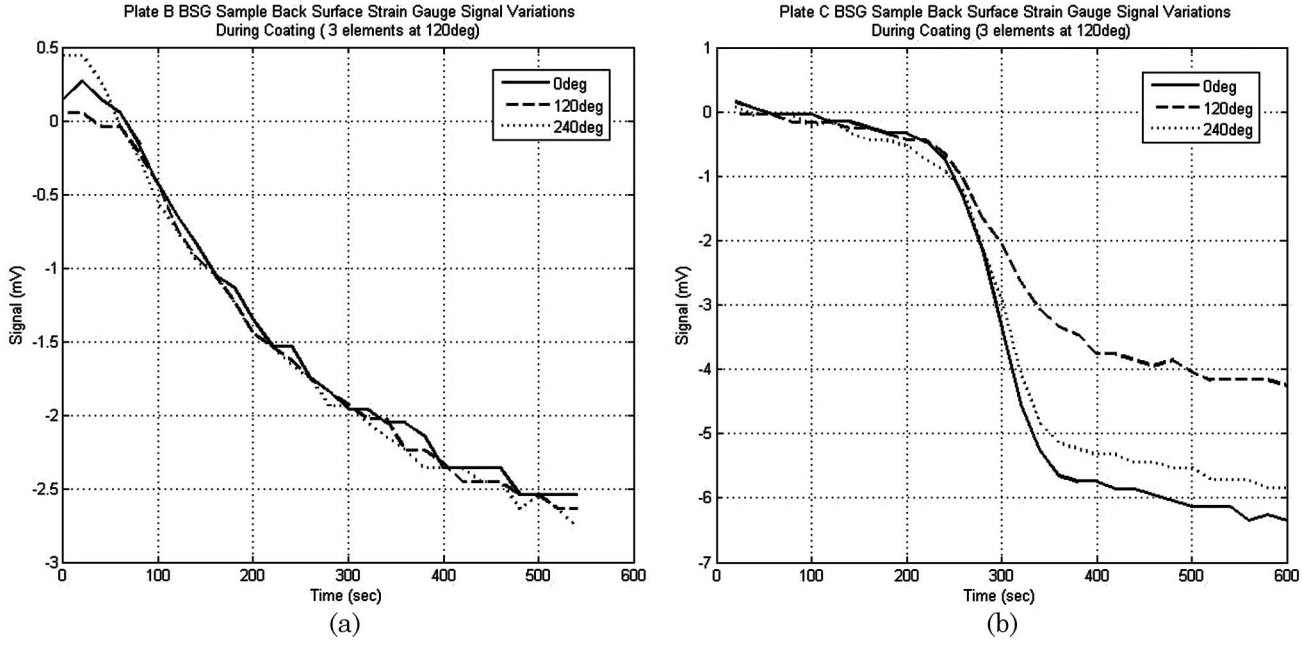

Fig. 6. Back-surface strain measurements for (a) plate B and (b) plate C.

strain gauge rosette. For the BSC sample on plate B [Fig. 6(a)], all three signals were very similar and resulted in a variation of ~3 mV. For the BSC sample on plate C [Fig. 6(b)], one of the elements had a weaker signal ~4 mV and the other two were ~7 mV. The principal strains can be calculated using the equations provided by the manufacturer, Vishay [11]. The maximum raw strain values obtained for the BSC sample are 6 μstrain on plate B and 14 μstrain on plate C.

B. Thermal Output Correction

The strain gauges are resistive sensors whose electrical resistance varies with temperature. To compute the real total strain, the raw signal from the strain gauges must be corrected for this thermal output using the thermal coefficients provided by the manufacturer. Five thermal polynomial coefficients were provided by the manufacturer over a temperature range of −250 °C to 450 °C. These coefficients produce large variations in thermal output correction over this whole temperature range. However, over the range of temperature of interest for this experiment, the thermal output curve is almost flat, incurring only small thermal output corrections between 5 and 10 μstrain (see Table 7).

After applying the thermal output correction, the total strain for the BSC sample becomes 1.3 μstrain on plate B and 4 μstrain on plate C.

C. Mechanical Strain

The strain gauge measures the total strain ε, the sum of the thermal strain and mechanical strain:

$$\varepsilon = \varepsilon_{\mathrm{Th}} + \varepsilon_M, \tag{5}$$

where ε is the total strain (μstrain) (corrected signal from strain gauge); $\varepsilon_{\mathrm{Th}}$ is the thermal strain (μstrain); and ε_M is the mechanical strain (μstrain).

The thermal strain, which is the product of the CTE and the temperature change [see Eq. (3)], is the inherent expansion of the glass from the increase of temperature. This strain is computed by multiplying the temperature change on the surface by the CTE of the borosilicate glass (2.8×10^{-6}/K). The measured temperature change on the back surface of the BSC sample is equal to 0.8 K for plate B and 2 K for plate C, so that the thermal strain reaches values of 2.2 μstrain for plate B and 5.6 μstrain for plate C.

The mechanical strain is a result of the physical resistance to the thermal expansion and is opposite in sign to the thermal strain. To determine the mechanical strain, the thermal strain is subtracted from the total strain measured by the strain gauges using the values computed above. After subtraction, ε_M reaches a value of −0.9 μstrain for plate B and −1.6 μstrain for plate C. The negative sign means here that the mechanical strain is in compression.

Table 7. Thermal Output Correction for Back-Surface BSC Sample on B and C Plates

	Temperature Range (°C)	Thermal Output Correction (μstrain)
Plate B	12.5/13.35	4.7
Plate C	14.6/16.6	10.0

D. Stress

The stress is the product of the mechanical strain and the Young's modulus $E = 8.5$ psi/μstrain (58.6 kPa/μstrain) for borosilicate glass. The stress values are summarized in Table 8.

The computed stress of less than 15 psi (0.1 MPa) on the back surfaces is well below the 100 psi (0.69 MPa) limit. Strain gauge measurements are not available for the top surfaces due to interference by the magnetron. However, since the temperature increase is concentrated on the exposed top surface and the temperature rise on the top surface is 2 to 3 times greater than on the back surface, the stress on the top surface should be of order 3 times the back-surface stress, according to the principle of through-the-thickness force and moment balance. Hence, we expect that, for the sample with a uniform thickness on plate B, the actual stress on the top surface would have been around 24 psi (0.16 MPa) for the 10 kW configuration. This result is in good agreement with the predicted actual stress of 23 psi (0.16 MPa) estimated above using the temperature model.

As presented earlier, a maximum predicted temperature rise of 4.5 °C was obtained for the 40 kW power level and of 2 °C for the 10 kW power level for the top surface of the LSST faceplate. A simple linear extrapolation suggests that the 40 kW case would produce a top surface actual stress of 54 psi (24 psi × 4.5 /2.0 = 54 psi) (0.37 MPa), which is well within the safe stress limit of 300 psi (2.1 MPa) for a polished optical surface. Likewise, the back surface should sustain an actual stress of order 12 psi (0.08 MPa), which is also well within the safe 100 psi (0.69 MPa) limit case of borosilicate glass (54 psi × 1/4.5 = 12 psi). Although this extrapolation is relatively simplistic, it is in good agreement with the back-surface strain measured values and shows that the actual stress is an order of magnitude less than the stress limits.

Table 8. Back-Surface Stress Computations from Measured Strain

	Thermal Strain (μstrain)	Total Strain (μstrain)	Mechanical Strain (μstrain)	Stress (psi)
Plate B	2.24	1.3	−0.94	−8
Plate C	5.6	4	−1.6	−14

7. Conclusion

A cast borosilicate mirror can be safely coated with sputtering. The measured temperature rise on the front and back surfaces were within the safe limits of cast borosilicate for the experimental coating thickness of 69 nm, utilizing a 10 kW magnetron. By utilizing the validated mathematical models, the temperature rise corresponding to variations of power, thickness, and coating times were investigated. These values were varied over the range anticipated for the LSST mirror application and, for every case, the resulting temperatures were within safe limits.

The strain on the weaker cast back surface of the sample was measured and was well within safe limits. Unfortunately, the magnetrons interfered with the strain measurements on the top surface; hence, direct measurements of the top surface strain were not available. The stress computed by extrapolating the strain measurement on the back surface to the top surface was shown to be also within safe limits because, since the top surface of the mirror will be polished, the material strength on the top surface will be much higher and less susceptible to thermal damage than the back surface.

The authors gratefully acknowledge the Gemini Observatory for allowing the execution of these tests in their coating chamber and deeply thank Tomislav Vucina and Clayton Ah Hee from the Gemini coating team for their help during the tests.

This material is based upon work supported by the National Science Foundation (NSF) under Cooperative Agreement AST-0809409.

References

1. V. Krabbendam, "The Large Synoptic Survey Telescope concept design overview," Proc. SPIE **7012**, 701205 (2008).
2. J. M. Hill, J. R. P. Angel, R. D. Lutz, B. H. Olbert, and P. A. Strittmatter, "Casting the first 8.4 m borosilicate honeycomb mirror for the Large Binocular Telescope," Proc. SPIE **3352**, 172–181 (1998).
3. J. Sebag, V. Krabbendam, G. Poczulp, D. Neill, T. Vucina, and M. Boccas, "LSST reflective coating studies," Proc. SPIE **6273**, 62730X (2006).
4. M. Boccas, T. Vucina, C. Araya, E. Vera, and C. Ah'Hee, "Coating the 8 m Gemini telescopes with protected silver," Proc. SPIE **5494**, 239–253 (2004).
5. M. Schneermann, M. Groessi, U. Nienaber, E. Ettlinger, J. A. Spiteri, and H. Clow, "Design and performance of the VLT 8 meter coating unit," Proc. SPIE **2871**, 136–144 (1997).
6. B. Atwood, D. Pappalardo, T. O'Brien, J. M. Hill, J. Mason, R. Belville, D. Steinbrecher, D. Brewer, E. Teiga, B. Sabol, J. Howard, and L. Miglietta, "The aluminizing system for the 8.4 meter diameter LBT primary mirrors," Proc. SPIE **6273**, 62730T (2006).
7. J. A. Thornton and J. E. Greene, "Sputter deposition processes," *Handbook of Deposition Technologies for Films and Coatings*, 2nd ed. (Noyes Publications, 1994), pp. 249–319.
8. W. B. Davison, J. T. Williams, and J. M. Hill, "Handling 20 tons of honeycomb mirror with a very gentle touch," Proc. SPIE **3352**, 216–224 (1998).
9. J. M. Hill, J. R. P. Angel, and B. Olbert, "Rules for handling large borosilicate honeycomb mirrors," Columbus Project Technical Memo UA-92-05 (Steward Mirror Lab, 1992).
10. J. R. Plaisted, G. McDonough, and G. Roche, "Effects of the anode configuration on substrate heating in dual magnetron sputtering," White paper SL-WHITE3-270-01 (Advanced Energy Industries Corporation, 2001).
11. Vishay Micro-Measurements, "Strain gage rosettes," Technical Note TN-515 (Vishay Micro-Measurements, 2008), http://www.vishay.com/strain-gages/knowledge-base-list/technotes-list/.